





Breakdown of the perfect crystal dynamics in dynamically disordered over-stoichiometric $\text{Nd}_2\text{NiO}_{4.25}$

A. Perrichon ^{1,*}, A. Piovano ^{2,†}, M. Boehm,² M. H. Lemée,² M. Ceretti ¹ and W. Paulus ¹

¹ICGM, Univ. Montpellier, CNRS, ENSCM, Montpellier 34000, France

²Institut Laue-Langevin, 71 Avenue des Martyrs, 38042 Grenoble, France



(Received 29 March 2022; revised 21 March 2023; accepted 22 March 2023; published 11 April 2023)

The lattice dynamics of oxygen-doped $\text{Nd}_2\text{NiO}_{4+\delta}$ is explored by a combination of single-crystal neutron spectroscopy, *ab initio* molecular dynamics (AIMD), and harmonic phonon calculations using density functional theory. The inelastic response computed from AIMD finds better correspondence with the experimental inelastic neutron spectra than the harmonic phonon calculations. The comparison of experimental and simulated data indicates that the presence of extra oxygen in interstitial sites leads to marked differences in the dynamics of the system compared to the stoichiometric parent compound. In particular, a nondispersive scattering signal was detected below 15 meV in all the experimental spectra in the (*ab*) plane. Its origin has been rationalized as an important incoherent scattering from Nd atoms, which emerges from in-plane atomic self-motions in the $\text{Nd}_2\text{O}_{2+\delta}$ rock-salt layers. The presence of additional interstitial oxygen atoms both dampens the long-range lattice dynamics as well as enhances oxygen and neodymium anharmonic displacements. The experimental observation of coherent and incoherent responses allows assessing the effect of interstitials on the vibrations of the whole crystal as well as on the dynamics of each atom independently.

DOI: [10.1103/PhysRevB.107.144303](https://doi.org/10.1103/PhysRevB.107.144303)

I. INTRODUCTION

Over-stoichiometric oxides of the rare-earth (*R*) nickelate family, $R_2\text{NiO}_{4+\delta}$ ($R = \text{La}, \text{Nd}, \text{Pr}$) and their doped forms, continue to attract interest due to their promising oxygen diffusion properties [1–19] as well as the intriguing magnetic properties and charge correlation effects they exhibit [20–25].

The $\text{Nd}_2\text{NiO}_{4+\delta}$ and $\text{Pr}_2\text{NiO}_{4+\delta}$ phases, in particular, have attracted much attention as they exhibit good oxygen ion conduction in the intermediate temperature regime of $T = 500\text{--}900$ K, high oxygen uptake, up to $\delta = 0.25$, and a high degree of chemical and mechanical stability, making them suitable electrode materials [2–5,9–11,14–17,26].

Disorder and dynamics due to overstoichiometry influence the oxygen mobility, but also the charge, spin, and lattice degrees of freedom. In $R_2\text{NiO}_{4+\delta}$ structures, the oxygen uptake is associated with modifications of both local and average structures. Moreover, the electronic changes due to the increasing amount of 3^+ valence state of the $3d$ metal, up to an equal amount of $\text{Ni}^{2+}/\text{Ni}^{3+}$ for $\delta_{\text{max}} \approx 0.25$, influences the magnetic interactions [20–22,27–30]. Some of the authors recently studied these interactions in detail in $\text{Pr}_2\text{NiO}_{4+\delta}$ [21], highlighting the formation of extra spin-wave side bands due to overstoichiometry, while any evidence of interaction in between lattice and spin was not found.

The structure of $\text{Nd}_2\text{NiO}_{4+\delta}$, shown as a scheme in Fig. 1, is layered and can be described as an intergrowth of square-

planar NiO_2 and rock-salt $\text{Nd}_2\text{O}_{2+\delta}$ layers. To facilitate the structural description, the oxygen atoms are labeled as *equatorial*, *apical*, and *interstitial* (see Fig. 1). Large anharmonicity of the displacements of the apical oxygen atoms constituting the rock-salt layers of $\text{Nd}_2\text{NiO}_{4.25}$ and $\text{Pr}_2\text{NiO}_{4.25}$ have been evidenced recently by means of single-crystal neutron diffraction [31], neutron spectroscopy on powder samples, and *ab initio* molecular dynamics (AIMD) simulations [18,19]. The pronounced displacements of the apical oxygen due to the presence of interstitials in their close proximity have been shown to contribute to the 2D oxygen diffusion in $R_2\text{NiO}_4$ -type oxide frameworks, even at moderate temperatures [32]. In particular, in $\text{Pr}_2\text{NiO}_{4.25}$, the strong anisotropic and anharmonic apical oxygen displacements evidenced at ambient temperature have been interpreted as enablers for a dynamically activated shallow oxygen diffusion pathway between apical and interstitial sites [31–33]. These findings are also supported by previously reported push-pull diffusion mechanism obtained from classical molecular dynamics (MD) on $\text{La}_2\text{NiO}_{4+\delta}$ and $\text{Pr}_2\text{NiO}_{4+\delta}$ at high temperature [34,35].

The disorder induced by the accommodation of excess oxygen in the rock-salt layer seems to play a crucial role for the general understanding of the oxygen mobility. We already proposed that a *phonon-assisted diffusion* might be an adequate model for oxygen mobility in $R_2\text{NiO}_{4+\delta}$ ($R = \text{La}, \text{Nd}, \text{Pr}$) in the intermediate temperature regime of $T = 500\text{--}900$ K [18,31]. Indeed, we have shown that thermally activated phonons promote oxygen displacements in the direction of the diffusion pathway, which in all likelihood leads to the periodic lowering of the elevated potential barriers for the diffusion of the double negative charged oxygen ions inside the crystal lattice. We now want to further develop the proposed

*Present address: ISIS Facility, STFC Rutherford Appleton Laboratory, Didcot OX11 0QX, United Kingdom.

†piovano@ill.fr

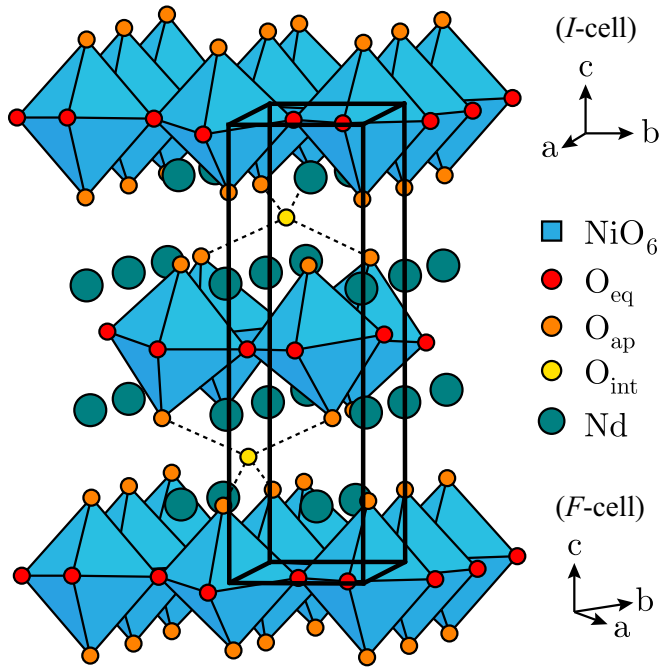


FIG. 1. Scheme of the $\text{Nd}_2\text{NiO}_{4+\delta}$ structure. Equatorial O_{eq} , apical O_{ap} , and interstitial O_{int} oxygen atoms are marked by red, orange, and yellow circles, respectively; neodymium atoms are marked by green circles; NiO_6 octahedra are colored in blue. Note that the insertion of O_{int} in the structure leads to pronounced displacements of the four first-neighbor O_{ap} (dashed lines), which, in first approximation, is accommodated by a tilting of the associated NiO_6 octahedra. The I cell used in the structural refinement is indicated by thick black lines. The reference axes of the I and F cells are indicated.

model and clarify the contributions of static or dynamic structural disorder, as well as the influence of local or long-range dynamics and their degree of correlation. The signature of static disorder shows up in diffraction patterns as diffuse scattering or superstructure peaks, while dynamic disorder should appear as quasielastic scattering or as a distinct feature, *a priori* not clearly defined, in the inelastic spectra [36]. The latter aspect is challenging to point out, as its signature is largely superimposed to dispersive bands.

While the detailed study of the impact of disorder on the dynamical response is uncommon in the field of ionic conductors, studies of self-dynamics inside the lattice as well as phonon anomalies associated with the materials' properties are better known in the fields of thermoelectrics or multiferroics [37–45]. As an example, the role of host-guest dynamics responsible for the low thermal conductivity in filled skutterudites has been the focus of a long debate that in the end pointed toward a collective motion origin of such effect [41,42,44]. More recently, a detailed description of phonon scattering responsible for such low thermal conductivity has been addressed with single crystal neutron spectroscopy through phonon lifetime measurements [37,38,45]. Other interesting classes of materials to mention here are the families of Cu_{2-x}X ($X = \text{S}, \text{Se}$ or Te) [46–48] and argyrodite materials [49] that show both superionic conduction as well as remarkable thermoelectric properties. Their flexible framework results in unusual low-energy phonon modes exhibiting very

strong anharmonic effects, which underlie both the superionic behavior and the ultralow thermal conductivity.

In this regard, single-crystal neutron spectroscopy experiments have the potential to address this challenge by measuring the anisotropic dynamic response of the sample as a function of energy $\hbar\omega$ and momentum transfers \mathbf{Q} along selected directions. The scattering function $S(\mathbf{Q}, \hbar\omega)$ is formally defined as the Fourier transform in time and space of the time-dependent pair-correlation function $G(\mathbf{r}, t)$ [50],

$$S(\mathbf{Q}, \hbar\omega) = \frac{1}{2\pi\hbar} \int G(\mathbf{r}, t) \exp\{i(\mathbf{Q} \cdot \mathbf{r} - \omega t)\} d\mathbf{r} dt, \quad (1)$$

where $G(\mathbf{r}, t)$ contains all information on the atomic motions. The scattering function is connected to the measured neutron spectra through the double differential cross section, which can be separated in coherent and incoherent parts.

In the coherent part of the scattering, the matrix elements for scattering by various atoms are added, and the sum is then squared, so the waves scattered by various atoms interfere. As a consequence, the cross section for scattering by the system as a whole is not equal to the sum of the cross sections for scattering by the individual atoms. Conversely, in the incoherent part of the scattering, the matrix elements are first squared and then summed, hence representing a sum over the cross sections for scattering by each atom. This does not mean that the scattering takes place as there were no other atoms. The self-correlation terms are determined by the properties of the system as a whole, but only by virtue of the chemical bond between them. This means that a proper choice of the composition of the sample would then give access to both coherent (total) and incoherent (self-) scattering functions.

To depict the details of the dynamics in intrinsically disordered materials, it is important to access both single-particle and lattice dynamics at specific $(\mathbf{Q}, \hbar\omega)$, which is achieved here by single-crystal measurements on a three-axis spectrometer. On one hand, the analysis of the coherent scattering gives important insights on the dynamics of the system as a whole. While coherent scattering contains a contribution from self-correlations, it is difficult to identify among all pair correlations. On the other hand, self-correlations are straightforwardly accessible from the analysis of incoherent scattering. However, oxygen itself shows only very weak incoherent scattering and, thus, contributes only marginally to the incoherent neutron spectra. The choice of a $3d$ metal and a cation with both sufficiently large incoherent cross sections would permit us to ascertain the effect of oxygen overstoichiometry on the atoms' self-dynamics in both perovskite and rock-salt structure subunits of the system.

While Ni naturally shows comparable coherent and incoherent scattering ($\sigma_{\text{coh}} = 13.3$ barns, $\sigma_{\text{inc}} = 5.2$ b), not all R are suited (Pr: $\sigma_{\text{coh}} = 2.46$ b, $\sigma_{\text{inc}} = 0.015$ b; Nd: $\sigma_{\text{coh}} = 7.43$ b, $\sigma_{\text{inc}} = 9.2$ b; La: $\sigma_{\text{coh}} = 8.53$ b, $\sigma_{\text{inc}} = 1.13$ b). Among all available R substitutes, Nd clearly is the one showing comparable incoherent and coherent scattering. In this material, the Nd in the rock-salt layer is acting, like Ni in the square-planar layer, as a sensor that can capture the effect of interstitial on self-dynamics. $\text{Nd}_2\text{NiO}_{4.25}$ is then the material of choice for a complete neutron spectroscopy investigation of the dynamics of the $R_2\text{NiO}_{4+\delta}$ phases.

Besides experimental measurements with neutron spectroscopy, the coherent and incoherent scattering functions can be obtained by first-principles methods. The coherent scattering function can be accurately derived from harmonic phonon calculations using density functional theory (DFT). However, this method does not account for potential anharmonicity and is limited to highly symmetric structural models with few inequivalent atoms. It is thus complicated to implement for nonstoichiometric phases with disorder that develops with temperature. It has been shown in previous studies by us and other authors that AIMD combined with a method to calculate the scattering function is well suited to investigate the lattice dynamics in disordered or diffusive compounds [18,19], since both coherent and incoherent scattering functions can be straightforwardly obtained at any temperature.

In this paper, we compare the coherent and incoherent scattering function computed from AIMD trajectories, at selected points in momentum space \mathbf{Q} , to detailed single-crystal inelastic neutron measurements from the thermal three-axis spectrometer IN8 at the Institut Laue Langevin (ILL, Grenoble). We show that the signatures on both self- and pair correlations appear in the measured neutron spectra, and demonstrate how the inclusion of excess oxygen atoms and subsequent disorder impacts both contributions.

II. EXPERIMENTAL

A. Sample preparation

The single crystal of $\text{Nd}_2\text{NiO}_{4.25}$ was grown using the traveling solvent floating zone technique, with a NEC SC3-MDH11020 mirror furnace in vertical configuration [51]. A picture of the as-grown single-crystal is shown in Fig. S1 of the Supplemental Material (SM) [52]. The crystal exhibits a pseudomerohedral twinning due to the phase transition from the high-temperature tetragonal (HTT) phase (space group $I4/mmm$, cf. I cell in Fig. 1) toward an orthorhombic symmetry, as for most nickelates of the $R_2\text{NiO}_{4+\delta}$ structural type and isostructural cobaltates and cuprates [31]. The transition temperature between the low- T orthorhombic and high- T tetragonal phase lies in the range 820–870 K. Furthermore, incommensurate satellites are observed at room temperature, associated with the long-range oxygen ordering of the interstitial oxide ions. All the subsequent analysis is performed on this high-quality, pure, and bulk single crystal, in which static defects (other than excess oxygen) and grain boundaries are in first approximation absent. Mass disorder from isotopic mixture is considered irrelevant in our measures since its effect is negligible given the instrument resolution. It follows that the contributions from the above-mentioned effects to the experimental data are negligible and thus cannot account for the experimental findings discussed hereafter.

B. Single-crystal neutron diffraction

The nuclear structure of $\text{Nd}_2\text{NiO}_{4.25}$ was investigated using neutron diffraction on the thermal neutron single-crystal diffractometer D19 at the ILL, using a wavelength of $\lambda = 0.95$ Å, at $T = 300$ K and 20 K. The experiment was performed on a $3.0 \times 2.8 \times 2.5$ mm³, once-twinned single

crystal of $\text{Nd}_2\text{NiO}_{4.25}$, cut along the crystal axis and mounted on a vanadium sample holder. Diffraction data were processed using SHELXL [53] to extract the average structure. By integrating together the Bragg reflections of the two twins, we obtain a pseudotetragonal structure with space group $I4/mmm$. To reflect the cell parameters of the real orthorhombic structure, the refined I cell is transformed into an F cell by the transformation matrix $[1 \ 1 \ 0, -1 \ 1 \ 0, 0 \ 0 \ 1]$. For structure refinement, we took into account the average structure only, i.e., F -type reflections, due to the complexity of the incommensurate modulation still under investigation. Additional $(hk0)$ diffraction maps have been collected on IN8 in the elastic configuration using the Flatcone multidetector setup with $k_i = k_f = 3$ Å⁻¹ [54]. The use of crystal analyzers reduced the background and allowed for the separation of static contributions from phonons within the given instrumental energy resolution of about 1 meV.

C. Inelastic neutron scattering

Lattice dynamics were measured at $T = 300$ K and 50 K on IN8. Pyrolytic graphite (PG) monochromator and analyzer were used together with $k_f = 2.662$ Å⁻¹. A PG filter was used to suppress harmonics, and a set of 30' collimators was employed to increase resolution. The instrumental \mathbf{Q} resolution of about 0.01 Å⁻¹, however, did not allow for differentiating the dynamics of twin domains from each another, hence we used average cell parameters with $a = b = 5.42$ Å and $c = 12.36$ Å with respect to the average F cell. This also means that, except from slight intensity differences due to weighting from the twin distribution, the $\mathbf{X}(\xi 00)$ and $\mathbf{Y}(0\xi 0)$ directions were considered being equivalent. We investigated two orientations of the crystal: the scattering plane formed by the $[110]$ and $[001]$ axes, and the one formed by the $[100]$ and $[010]$ axes. This gave access to the $\mathbf{X}(\xi 00) = \mathbf{Y}(0\xi 0)$, $\mathbf{M}(\xi\xi 0)$ and $\mathbf{Z}(00\xi)$ directions in both longitudinal and transverse setup.

The single crystal used for the experiment was a two-times twinned cylindrical crystal of length 20 mm and diameter 6.5 mm. The choice of the sample size was thought to be a good compromise between a reasonable level of multiple scattering and a statistically relevant single-scattering signal. A calculation of scattering probability for our sample shape gives a contribution of multiple scattering with respect to single scattering of about 15%. The possible contribution of multiple scattering to the shape of experimental data cannot be then excluded *a priori*. Most advanced calculations for the multiple-scattering contributions assume isotropic scattering that might not be appropriate in the case of an oriented single crystal. Furthermore, such calculations are often based on Monte Carlo methods that require as an input a functional form of the $S(\mathbf{Q}, \hbar\omega)$, which is actually the unknown of this investigation. We here decided to deal with this issue by calculating the single scattering coherent and incoherent dynamical structure factors directly from AIMD, presently one of the best theoretical methods to retrieve these functions, and compare them to the experimental data. The comparison of the contributions of single-scattering events over experimental data helped shed light *a posteriori* on the real contribution of multiple scattering.

D. Computational methods

All *ab initio* simulations were performed within the DFT framework, using a plane-wave pseudopotential approach as implemented in VASP [55–58]. The ionic core-valence interaction is described using the projected augmented wave method [59,60]. For the exchange-correlation part, we used the generalized gradient approximation, together with the Perdew-Burke-Ernzerhof pseudopotentials [61]. The Gaussian smearing method was chosen to describe partial occupancy of orbitals, with a small smearing width of $\sigma = 0.05$ eV. For MD simulations, we used only Γ -point Bloch functions, but for static calculations and relaxation, the Brillouin zone was sampled using a $2 \times 2 \times 1$ k -point mesh. The calculations were converged to energies within 10^{-7} eV for the electronic structure and to forces within 10^{-3} eV/Å for the ionic relaxations.

AIMD simulations were performed on the $\text{Nd}_2\text{NiO}_{4.25}$ and $\text{Nd}_2\text{NiO}_{4.0}$ phases using, respectively, $2\sqrt{2} \times 2\sqrt{2} \times 1$ and $2 \times 2 \times 1$ supercells with respect to the F cell. The structural model of $\text{Nd}_2\text{NiO}_{4.25}$ contains a total of 232 atoms representing 32 Nd_2NiO_4 units and eight extra oxygen atoms to reach the overstoichiometry of $\delta = 0.25$. The excess oxygen atoms in interstitial sites (O_{int} in Fig. 1) are positioned far enough from each other so the overall distortion of the structure is minimized. In particular, the designed structure is intended to avoid the highly energetic configurations where the four next-neighbor apical oxygen atoms surround the interstitial (see dashed lines in Fig. 1), and by extension the four octahedra in which they belong, are affected by multiple interstitials. More details on the design of the nonstoichiometric structural model is available in the SM [52]. In the stoichiometric $\text{Nd}_2\text{NiO}_{4.0}$ case, the model contains 112 atoms, representing 16 formula units.

The trajectories were obtained using the velocity Verlet algorithm with a time step of 2 fs. The temperature was kept to a set value during the simulation using a canonical ensemble by coupling the system to a Nose-Hoover thermostat [62–64]. The AIMD were performed at $T = 150$ K and 310 K. The structural models were first geometry optimized then equilibrated with AIMD over 2 ps. Exploited data consist of 40-ps-long trajectories. We carefully checked the possibility for coupling effects in between the thermostat and the system and we have not found any artifact with the used parameters.

The incoherent and coherent scattering functions were computed from the AIMD trajectories using the MDANSE software [65]. Additional analyses of the trajectories were performed with the positional recurrence maps (PRM) code [19].

The coherent scattering function has also been calculated by finite displacement phonon calculations from DFT to support the output from AIMD. Calculations were performed using the direct method by computing the Hellmann-Feynman forces on the $\text{Nd}_2\text{NiO}_{4.0}$ low-temperature phase, using a $2 \times 2 \times 1$ supercell of the F -cell structural model containing four formula units. As in our previous study [18,19], collinear magnetism has been added for Ni ions only, which results in a symmetry lowering from tetragonal to orthorhombic and improves the matching of theoretical cell parameters with respect to experimental ones. The dynamical matrix diagonalization

and the calculations of phonon dispersion curves and phonon intensities are performed with PHONON [66].

III. RESULTS AND DISCUSSION

A. Structure of $\text{Nd}_2\text{NiO}_{4.25}$

The average crystallographic structures of $\text{Nd}_2\text{NiO}_{4.25}$, obtained from single-crystal neutron diffraction refinements at $T = 300$ K and 20 K are reported in Table I. The analysis confirms the expected strong delocalization of apical oxygen atoms O_{ap} in the (ab) plane, at both temperatures, in agreement with previous studies [31].

We repeated the diffraction experiment within the ($hk0$) plane at 300 K and 1.5 K on IN8, taking advantage of the large angle analyzer system FlatCone. The ($hk0$) scattering planes at 300 K and 1.5 K are reported in Fig. S2 in the SM [52]. Similar to previous diffraction experiments on $\text{Nd}_2\text{NiO}_{4.25}$ [31], many satellite peaks appear all around the average structure peaks (with symmetry $F4/mmm$), which indicate a long-range incommensurate structure. However, given the large number of incommensurate peaks, the structure approximates a completely disordered one. The only modification of the diffraction pattern occurring in between 300 K and 1.5 K is an increase of the satellite intensities with lowering the temperature. We remark that no lock-in transition to a commensurate structure takes place for $\text{Nd}_2\text{NiO}_{4.25}$.

Incommensurate phases are predicted to have specific dynamics associated with the loss of translation symmetry. In the case of small incommensurate distortions with respect to the high-symmetry phase, the extra dynamics can be described in terms of phase and amplitude modes (phasons and amplitudons) [67,68]. In particular, the phase mode has an acousticlike dispersion, emerging from the satellites. Inelastic neutron scans through several incommensurate peaks in $\text{Nd}_2\text{NiO}_{4.25}$ did not evidence specific signatures of phason modes (see Fig. S3 in the SM) above 1 meV energy transfer [52]. It follows that the phason modes, if present, are too low in energy to have a major influence on the overall oxygen dynamics or are overdamped and hidden in the elastic incoherent line.

B. Dispersion curves and coherent scattering

The experimental dispersion curves of $\text{Nd}_2\text{NiO}_{4.25}$, reconstituted from IN8 data along several high-symmetry directions, are shown in Fig. 2, together with the simulated dispersion curves from harmonic phonon DFT calculations for the parent $\text{Nd}_2\text{NiO}_{4.0}$ (black lines in Fig. 2). Phonon energies and phonon line widths are extracted through a fit to the data. The data points, represented as markers with error bars corresponding to the fitted phonon line widths, are color coded depending on the polarization of the measurements: longitudinal (red circles), transverse (blue circles), and mixed, where both longitudinal and transverse are visible (green circles).

All our attempts at DFT-based harmonic phonon calculations for the overstoichiometric structures were unsuccessful. This is due, on one hand, to the symmetry loss from the F -cell description when incorporating excess oxygen atoms into specific interstitial sites, and on the other hand to the shallowness of the apical oxygen atom potentials, which is also

TABLE I. (top) Neutron single-crystal structure refinement of $\text{Nd}_2\text{NiO}_{4.25}$ at $T = 300$ K (D19@ILL, $\lambda = 0.95$ Å); average space group: $I4/mmm^a$, $a = b = 3.8235(5)$ Å, $c = 12.3440(25)$ Å; $R = 0.0840$, $R_W = 0.0785$. (bottom) Neutron single-crystal structure refinement of $\text{Nd}_2\text{NiO}_{4.25}$ at $T = 20$ K (D19@ILL, $\lambda = 0.95$ Å); average space group: $I4/mmm^a$, $a = b = 3.8172(5)$ Å, $c = 12.3032(25)$ Å; $R = 0.1103$, $R_W = 0.0987$.

Atom	x	y	z	Occupancy	U_{iso}	U_{11}	U_{22}	U_{33}
Nd	0	0	0.3585(5)	2		0.0113(26)	0.0113(26)	0.0057(30)
Ni	0	0	0	1		0.0039(26)	0.0039(26)	0.0122(35)
O _{eq}	0.5	0	0	2		0.0008(56)	0.0155(65)	0.0615(72)
O _{ap}	0	0	0.1716(10)	2		0.119(11)	0.119(11)	0.0132(58)
O _{int}	0.5	0	0.25	0.304(72)	0.049(2)			
Nd	0	0	0.3590(3)	2		0.0078(8)	0.0078(8)	0.0033(12)
Ni	0	0	0	1		0.0012(7)	0.0012(7)	0.0072(13)
O _{eq}	0.5	0	0	2		0.0027(17)	0.0057(18)	0.0617(52)
O _{ap}	0	0	0.1717(6)	2		0.1069(69)	0.1069(69)	0.0020(27)
O _{int}	0.5	0	0.25	0.258(64)	0.05			

^aThe structure data are given in $I4/mmm$ (I cell) while the discussion in the paper is focused on $F4/mmm$ (F cell). Both descriptions are fully equivalent. Since the diffusion pathway between apical and interstitial sites goes along $[110]$ in the F cell, which is corresponding to $[100]$ in the I cell, it is easier to estimate the displacement factors of the apical oxygen and Nd atoms as all mixed U_{ij} become zero in the I -cell description. In such a way, the average displacement corresponds to the RMS value of the respective U_{ii} (in Å² units).

at the origin of their large atomic displacement parameters (ADPs) (see Table I). Indeed, a shallow potential makes the computation of the atomic forces and thus of the dynamical matrix problematic, leading to incorrect phonon dispersion curves with numerous imaginary modes. The fact that the minimal supercell structure used to account for interstitial is not able to reproduce the dynamics of such a phase is clear proof of the complexity of this structure and, in particular, of the interplay in between disorder and substructure order at different length scales.

Hence, reliable phonon dispersion relations with non-negative eigenvalues could only be obtained for the low temperature ($T < 130$ K) $\delta = 0$ tetragonal phase with $P4_2/nm$ symmetry, known as the low-temperature tetragonal phase (LTT). An overview of the dispersion along principal symmetry directions in the full energy range is available in Fig. S4 of the SM [52]. The experimental data are of the orthorhombic $\delta = 0.25$ phase, which is averaged due to the twinning into the above-mentioned tetragonal $F4/mmm$ structure. Bearing in mind this limitation, the DFT results turn out to be sufficient for a qualitative analysis and for assigning some of the experimentally observed modes to specific phonon branches.

We first point out that, in the out-of-plane Γ - Z direction [Fig. 2(c)], the measured data points follow accurately the calculated dispersion curve of the $\delta = 0$ phase. Error bars in Fig. 2, which indicate phonon line widths, are resolution limited in this direction. We can thus assert that excess oxygen atoms have negligible effects on the low-energy lattice dynamics along the stacking-axis c direction.

By contrast, the two in-plane directions present a more puzzling picture. Figures 2(a) and 2(b) show the Γ - X and Γ - M directions, which were measured in different Brillouin zones. The overall dispersion of low energetic in-plane excitation does not find the same close correspondence with harmonic phonon DFT calculations. The acoustic branches, dispersing out from the zone center, still show reasonable agreement with the calculations until $\xi \approx 0.25$ r.l.u., with a

slight stiffening of the longitudinal acoustic mode along $[100]$ [Fig. 2(a), red points] compared to the $\delta = 0$ calculations. This stiffening is rationalized by the presence of the interstitial oxygen atoms, which harden the interaction potential along $[100]$. Nevertheless, above $\xi \approx 0.25$ r.l.u., the acoustic phonons flatten and become broadened up to the Brillouin zone borders. This corresponds to the merging of the acoustic branch with a dispersionless broad optical excitation. Here the correspondence between calculated and measured frequencies of the individual branches becomes quite poor. Such phonon dispersion of longitudinal acoustic branches along $[100]$ and $[110]$ directions show some similarity with the acoustic mode dispersion found in other incommensurate phases [69]. At higher energies, other broad dispersionless opticlike excitations are observed.

The large line widths of the phonon branches can indicate a reduced lifetime of the associated phonons (homogeneous broadening), which can be a direct consequence of the presence of interstitial excess oxygen atoms or of anharmonic atomic potentials, or can indicate a spread in local structural environments (inhomogeneous broadening), which are each associated to slightly different phonon frequencies. Furthermore, the broadening can also be a consequence of the twinning of the single crystal.

To have a look at this last possibility, we decomposed in Fig. S5 of the SM the contribution of phonons calculated from AIMD at the zone boundary along the two orthogonal directions, i.e., along the Γ - X and Γ - Y directions of the real orthorhombic structure [52]. These two contributions represent the calculated difference of phonon spectral lines from the two twins of the structure. We can see minor differences in the spectral weight of the components of the two twins: the low-energy component is mostly connected with incoherent scattering and the upper component with coherent scattering. Focusing on the later contribution, we can see from Table S1 in the SM that the resolution-deconvoluted peak width and position barely change in between the two twins [52].

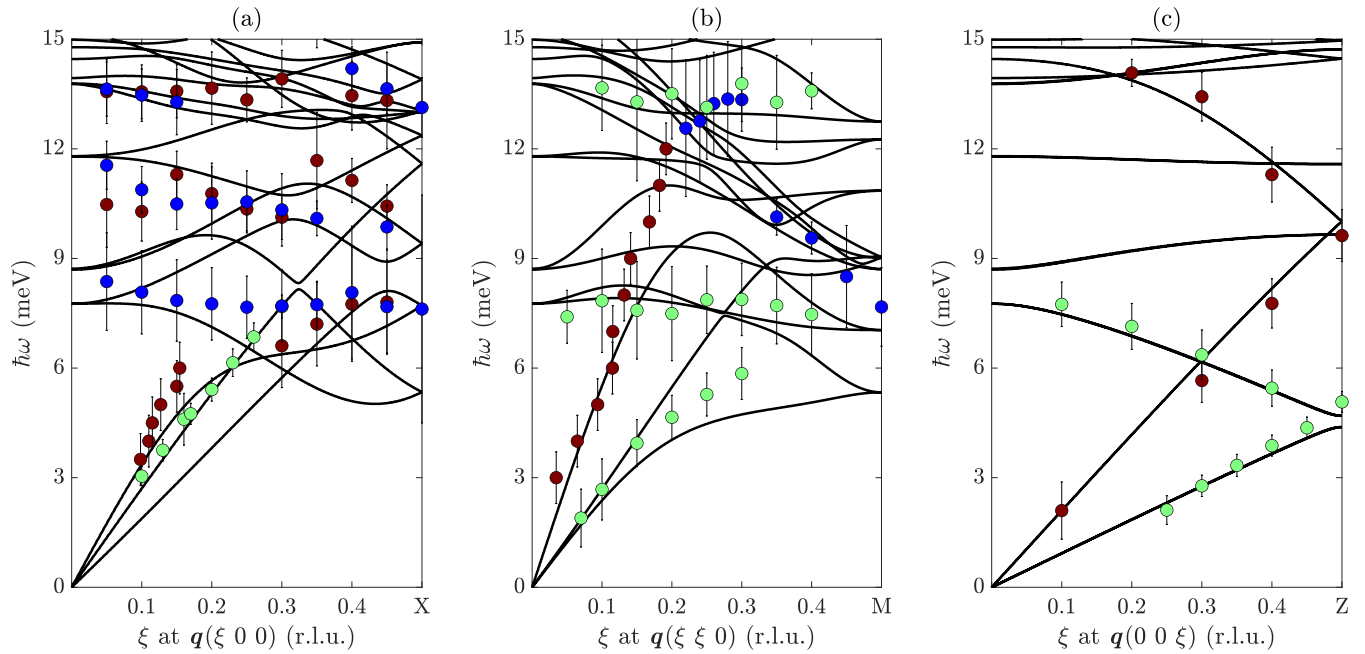


FIG. 2. Measured dispersion curves for $\text{Nd}_2\text{NiO}_{4.25}$ for the directions (a) Γ - \mathbf{X} (superimposed to Γ - \mathbf{Y} by twinning), (b) Γ - \mathbf{M} , and (c) Γ - \mathbf{Z} . Data points and error bars, which, respectively, represent the energy and the full width at half maximum (FWHM) of the measured phonon excitations, are extracted through a fit of the IN8 data, including measurements at both 50 K and 300 K. Data points are color coded depending on the geometry of the measurements, being sensitive to purely longitudinal (red), purely transverse (blue), or displacements of both kinds (green). Note that data points with $\xi > 0.5$ are mirrored with respect to the zone boundaries of the simulation cell. Black lines represent the calculated dispersion curves from harmonic phonon DFT calculations of $\text{Nd}_2\text{NiO}_{4.0}$.

The averaged tetragonal approximation of the contributions, reported in Fig. S5(f) of the SM, shows a peak width of about 6 meV that compares well with the experimental one of about 5 meV [52]. In comparison, the line width from DFT within the harmonic approximation is only 1.5 meV. This clearly points out that most of the contribution to the peak broadening comes from anharmonicity, inherently included in MD simulations, and marginally from twinning.

The correspondence between DFT of the LTT phase and measurements of $\text{Nd}_2\text{NiO}_{4.25}$ definitely breaks down by comparing the phonon intensities, instead of their frequencies, as shown in Fig. 3. Experimental data measured at $T = 50$ K around the $(1\ 4\ 0)$ Brillouin zone are represented in the form of a color map in Fig. 3(a), while the coherent neutron scattering intensities, calculated by DFT and convoluted to the experimental resolution, are shown in Fig. 3(b), together with the dispersion curves.

The strong intensity observed in the experimental data around \mathbf{X} $(0.5\ 4\ 0)$ near 11–13 meV, which is associated to an acoustic phonon mode dispersing from $(0\ 4\ 0)$, is well reproduced in the DFT calculations. We note, however, that this mode weakens considerably above $(0.8\ 4\ 0)$ in the experimental spectra, while the simulation predicts considerable spectral weight up to $(1\ 4\ 0)$. We also observe a mode at 12 meV at Γ that disperses down to 10 meV going toward \mathbf{X} before being subsided by a spurion. Another low-lying mode at 7–8 meV, barely dispersive, was detected, where the intensity, however, does not correspond to that predicted by harmonic phonon calculations.

Table S2 in the SM lists the expected atomic displacements, obtained from DFT, at the \mathbf{X} zone boundary in the

energy range up to 16 meV [52]. The low energetic dynamics is exclusively due to various Nd-O in-plane displacements, e.g., the low-energy optic modes around $\hbar\omega = 8$ meV are mostly sliding motions in the (ab) plane, and concern the neodymium and apical oxygen atoms.

In addition to phonon scattering, we observed that a broad, diffuse intensity, from the elastic line and up to $\hbar\omega = 15$ meV, is present in the experimental spectra for all in-plane directions Γ - \mathbf{X} (Γ - \mathbf{Y}) and Γ - \mathbf{M} , in every measured Brillouin zone. This diffuse feature is not accounted for by the coherent scattering function of the LTT phase, which thus suggests that either it originates from a deeply modified lattice dynamics in the in-plane directions due to the presence of excess oxygen or it corresponds to some scattering other than one-phonon coherent scattering.

One of the possibilities might be an important contribution from multiphonon scattering. Taking into account the atomic displacement amplitude at 50 K and the \mathbf{Q} values of interest, we could estimate the contribution of the multiphonons to be less than 7%. We can thus safely assert that one-phonon scattering is the predominant contribution to the spectral intensity.

C. Incoherent scattering

The AIMD method, which outputs atomic trajectories, here provides a direct means to calculate the scattering function without assuming the shape of the atomic potential, at the difference of the direct-method discussed above that assumes harmonic atomic potentials. The major drawback of this AIMD method is the limitation of the size of the supercells due to the rapid increase of the computing effort with the

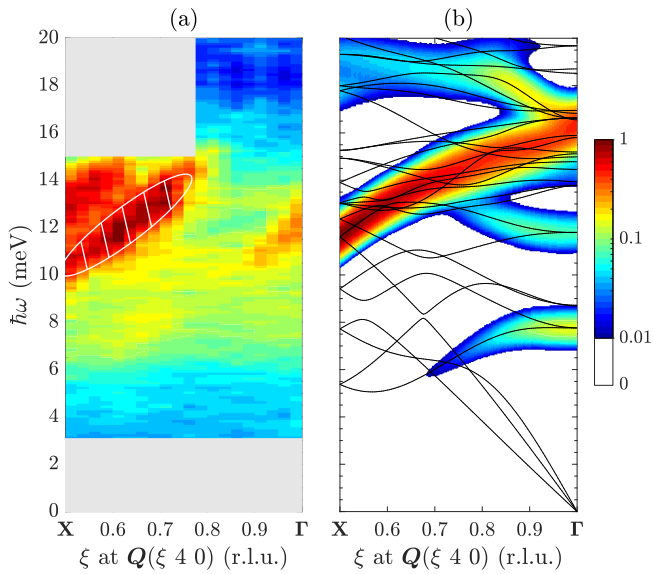


FIG. 3. (a) Color maps of IN8 experimental scans on the $\text{Nd}_2\text{NiO}_{4.25}$ single crystal along Γ - X (superimposed to Γ - Y by twinning). The experimental intensities are corrected by the Bose-Einstein factor, and shown in logarithmic scale. An interpolation by a factor of 2 is applied in both energy and momentum transfer. The measurements were done around the $(1\ 4\ 0)$ Brillouin zone at 50 K. Intensity in the white shaded area is given by a spurious peak originating from accidental Bragg scattering. (b) Color maps of the coherent scattering function convoluted to the instrument resolution and with intensity in logarithmic scale, calculated from harmonic phonon DFT calculation for $\text{Nd}_2\text{NiO}_{4.0}$. Full lines correspond to the calculated dispersion curves.

number of atoms. As it is a real space method, the number of accessible momentum points \mathcal{Q} in reciprocal space is limited to the Γ points and a few other points in the (ab) plane, of interest here the zone boundaries X $(0.5\ 0\ 0)$, Y $(0\ 0.5\ 0)$, and M $(0.5\ 0.5\ 0)$. To reproduce the effect of the twinning in the experimental data, the scattering functions calculated from the AIMD method are averaged for symmetry-equivalent \mathcal{Q} vectors (see Fig. S6 and Table S3 in the SM for the list of equivalence [52]).

Figure 4(a) shows the experimental spectra (black line and markers) measured at the point X $(0.5\ 4\ 0)$. The spectrum consists of three distinctive parts: (1) the usual elastic line at the energy transfer $\hbar\omega = 0$ meV generated by incoherent elastic scattering, (2) a resolution limited excitation at $\hbar\omega = 13$ meV (the 11 meV signal is spurious), and (3) the broad diffuse feature discussed in Fig. 3, from the elastic line and up to $\hbar\omega = 15$ meV. The spectrum is compared to the coherent scattering function from DFT (blue line) and the total scattering function from AIMD (green line) convoluted to the experimental resolution, and arbitrarily scaled. The DFT spectra exhibits an excitation at $\hbar\omega = 12$ meV, which is the counterpart of the mode measured at $\hbar\omega = 13$ meV. The analysis of the atomic displacements associated with the phonon modes at X for the $\delta = 0$ case gives four distinct movement patterns in this energy range (see Table S2 in the SM [52]). As mentioned earlier, the (coherent) DFT spectra does not account for the broad diffuse feature observed

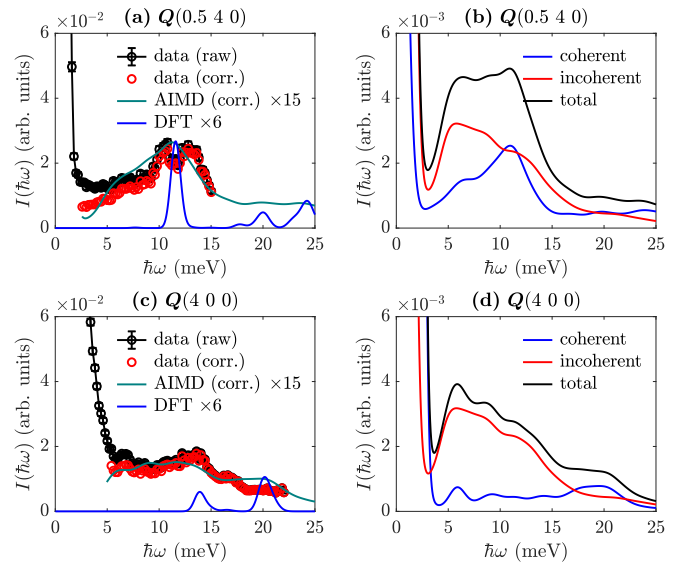


FIG. 4. (a), (c) Energy scans at \mathcal{Q} $(0.5\ 4\ 0)$ and \mathcal{Q} $(4\ 0\ 0)$, respectively, measured on the $\text{Nd}_2\text{NiO}_{4.25}$ single crystal at $T = 50$ K on the triple-axis spectrometer IN8. Black markers and line represent the raw experimental data, and the red markers the experimental data after correction by the Bose-Einstein factor. The coherent scattering function of $\text{Nd}_2\text{NiO}_{4.0}$, calculated by DFT, are represented by blue lines. The total (coherent plus incoherent) scattering functions multiplied by the scattering cross section of $\text{Nd}_2\text{NiO}_{4.25}$, calculated by AIMD at 310 K, are represented as green lines. Note that the AIMD spectra in (a) and (c) have been corrected to account for the temperature dependence of the intensities using the Bose-Einstein factor. (b), (d) Corresponding scattering functions of $\text{Nd}_2\text{NiO}_{4.25}$, calculated by AIMD at 310 K (without the empirical correction for the temperature), at \mathcal{Q} $(0.5\ 4\ 0)$ and \mathcal{Q} $(4\ 0\ 0)$, respectively. The coherent, incoherent, and total scattering functions multiplied by the respective neutron cross sections are represented as blue, red, and black lines, respectively.

experimentally. As for the AIMD spectra, it is in much better agreement with the experimental data (red markers) and accounts for both the excitation near $\hbar\omega = 13$ meV and the broad diffuse feature.

Figure 4(b) shows the coherent and incoherent contributions of the total scattering function calculated from AIMD and represented in Fig. 4(a). We first notice that the intensity of the coherent and incoherent scattering functions is comparable. The coherent scattering function (blue line), exhibits one strong, broad phonon mode at $\hbar\omega = 12$ meV, which is in good agreement with the result from harmonic phonon DFT calculations. While no Bragg peak is expected at $(0.5\ 4\ 0)$, the AIMD predicts some weak coherent elastic intensity, which can either be an artifact due to the periodic conditions of the supercell or the signature of static spatial correlations emerging from the disorder induced by the presence of randomly arranged excess oxygen atoms. The diffraction pattern in Fig. S2 in the SM [52], however, suggests that the excess oxygen is incommensurately ordered with respect to the average structure at 300 K. The real effect of excess oxygen arrangement on elastic scattering cannot be accurately captured in the simulations of our relatively small supercell. The incoherent scattering function (red line) gives the

expected contribution at $\hbar\omega = 0$ meV but also a broad inelastic signal centered at about 8 meV, in good agreement with the experimentally observed signal. The total scattering function (black line) shows an agreement with the experimental data far better than that obtained from harmonic phonon DFT calculations when considering only the coherent scattering function. This suggests that a significant part of the observed spectral weight is due to incoherent processes.

The importance of correctly considering the inelastic incoherent contribution is even more striking for the Γ point (4 0 0), where only weak coherent inelastic scattering is expected from calculations as shown in Fig. 4(d), although the experiment shows strong intensity in the entire range up to 18 meV [Fig. 4(c)]. The calculated incoherent inelastic contribution dominates this region and gives a clear explanation to this experimental finding at this point. We emphasize that the spectra calculated from the AIMD correspond to first order and a single scattering event. Given the satisfactory accord of these theoretical spectra to the experimental features, we can be finally confident that the real contribution of multiple-scattering events are not predominant in defining the spectral shape in the plotted energy region.

Figure 5(a) presents the calculated incoherent scattering function split into the individual atomic contributions of nickel, neodymium, and oxygen, correctly weighted to reflect the stoichiometry. To separate the spectral shape of the scattering function and the spectral weight introduced by the neutron cross section, the partial incoherent scattering functions are shown both before (dashed lines) and after (full lines) weighting by the neutron incoherent cross-sections. Note that given the choice of \mathbf{Q} (2.5 2 0), only the modes polarized in the (ab) plane may contribute to the signal. We observe that the partial incoherent scattering function of the oxygen, projected on the (ab) plane, is as significant as that of Nd. However, taking into account the incoherent cross section of the oxygen of $\sigma_{\text{O,inc}} = 0.000(8)$ barn compared to Nd, $\sigma_{\text{Nd,inc}} = 9.2(8)$ barn and Ni, $\sigma_{\text{Ni,inc}} = 5.2(4)$ barn, the effective contribution of the oxygen atoms to the incoherent double differential cross-section is negligible. As such, the measured incoherent signal on the (ab) plane is dominated by the neodymium contribution only. The lack of significant contribution from Ni in Fig. 5 is due to the Ni displacements being polarized mainly in the c direction, which is supported also by the elongated ADPs of Ni in the c direction (see Table I). Similarly, the displacement and the ADP of the equatorial oxygen is also mainly in the c direction. The fact that, at comparable incoherent cross sections, the spectral weight comes from Nd and not from Ni clearly points out that the incoherent scattering emerges from the (ab) plane and, hence, that the corresponding self-dynamics is emerging from the $\text{Nd}_2\text{O}_{2+\delta}$ rock-salt layer and not from the NiO_2 layer.

In Fig. 5(b), we show the partial incoherent scattering functions for $\text{Nd}_2\text{NiO}_{4.0}$. Since the total scattering intensity depends on the number of atoms and their total neutron cross sections, which is similar between the $\text{Nd}_2\text{NiO}_{4.0}$ and $\text{Nd}_2\text{NiO}_{4.25}$ formula units, similar incoherent scattering intensity for the $\delta = 0.25$ and $\delta = 0$ phases is observed. As for the $\delta = 0.25$ phase, the incoherent scattering for the $\delta = 0$ phase along the (ab) plane is dominated by the contribution of the neodymium, however, with a markedly different spectral shape.

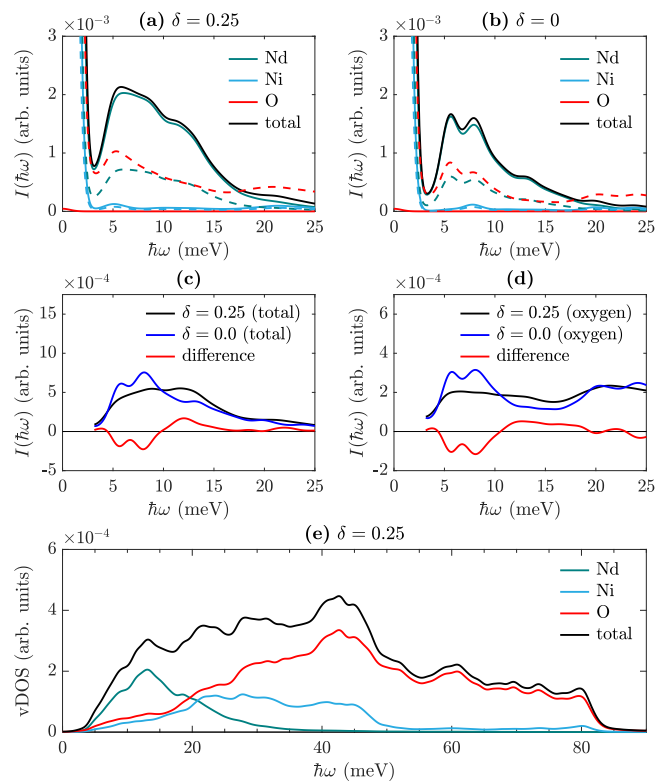


FIG. 5. (a), (b) Partial incoherent scattering functions of Nd (green), Ni (blue), and O (red), calculated for the full simulation cells from AIMD at \mathbf{Q} (2.5 2 0) for (a) $\text{Nd}_2\text{NiO}_{4.25}$ at $T = 310$ K and (b) $\text{Nd}_2\text{NiO}_{4.0}$ at 150 K. Dashed lines are self-part of the scattering function $S_s(\mathbf{Q}, \hbar\omega)$, while full lines are the results of weighting $S_s(\mathbf{Q}, \hbar\omega)$ with the incoherent neutron cross sections. (c), (d) Comparison at \mathbf{Q} (2.5 2 0) between (c) the total incoherent scattering functions, and (d) the self-correlations for the oxygen only, of $\text{Nd}_2\text{NiO}_{4.25}$ (black) and $\text{Nd}_2\text{NiO}_{4.0}$ (blue). Each set of data is corrected by the Bose-Einstein factor. The difference of the $\delta = 0.25$ and $\delta = 0$ spectra is indicated in red. (e) Partial and total vibrational vDOS of $\text{Nd}_2\text{NiO}_{4.25}$, calculated from AIMD at 310 K for isotropic scattering, weighted by the respective scattering cross sections.

To better appreciate this, the incoherent scattering functions of the $\delta = 0.25$ (black line) and $\delta = 0$ (blue line) phases, corrected by the Bose-Einstein factor, is compared in Fig. 5(c). Considering the inelastic incoherent scattering originating from isotope and spin-nuclear contributions, which results equivalently in Nd_2NiO_4 and $\text{Nd}_2\text{NiO}_{4+\delta}$, the modification of the inelastic scattering between the $\delta = 0.25$ and $\delta = 0$ phases depends solely on the underlying modification of the self-correlations. By subtracting the spectra of the $\delta = 0$ phase from that of the $\delta = 0.25$ phase [red line in Fig. 5(c)], we evidence a partial shift of spectral weight from modes around $\hbar\omega = 5.5$ meV and 8.0 meV, toward modes in the range $\hbar\omega = 11$ –15 meV. A similar trend is observed when considering the difference of the partial contribution of the oxygen atoms of the $\delta = 0$ and $\delta = 0.25$ phases, as shown in Fig. 5(d).

This shift in spectral weight toward higher energy is consistent with the stiffening of the lattice modes in the (ab) plane (see Fig. 2). However, the picture is more complex than this since not all the spectral weight of Nd vibrations is transferred

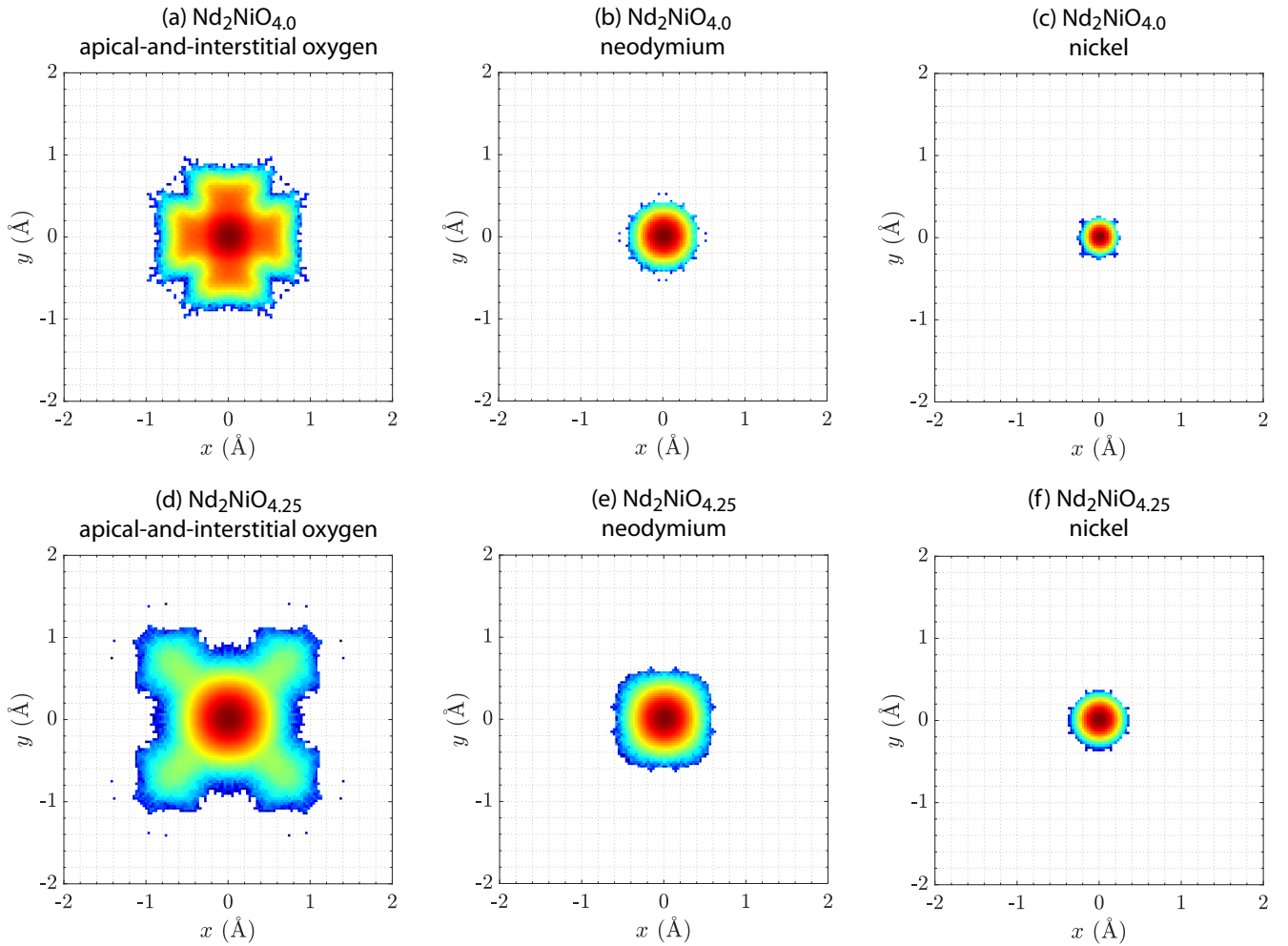


FIG. 6. Histogram of atomic displacements projected in the (ab) plane, calculated from the AIMD trajectories using the PRM method for $\text{Nd}_2\text{NiO}_{4.0}$ (a)–(c) and $\text{Nd}_2\text{NiO}_{4.25}$ (d)–(f) at $T = 310$ K. Apical-plus-interstitial oxygen (a), (d); neodymium (b), (e); and nickel (c), (f).

to higher energies. The well-defined double peak incoherent signal at 6–8 meV for the stoichiometric case is smeared over a broad range of frequencies in the overstoichiometric case, without any evident sharp feature left. The distribution of vibrational modes of Nd in the (ab) plane has then changed due to the overstoichiometry. This change can be rationalized considering that Nd atoms close to interstitial oxygen atoms feel a modified potential, due to steric hindrance, which favors vibrational modes at higher energies.

For the sake of clarity, the total and partial vibrational density of states (vDOS) of $\text{Nd}_2\text{NiO}_{4.25}$ from AIMD for isotropic scattering (i.e., powder average) are reported in Fig. 5(e) in the full energy range. The plot shows that vibrational modes extend up to around 80 meV, as experimentally found [18], and also calculated through DFT finite displacement approach (Fig. S4 in the SM [52]). Moreover, the vDOS highlights that the main contribution to the spectral weight below 20 meV comes from the Nd atoms. Note that the vDOS of Fig. 5(e) is calculated in the isotropic approximation, and thus includes a mode polarized in the c direction, while the incoherent scattering functions of Figs. 5(a)–5(d) only contain contributions in the (ab) plane.

The presence of excess oxygen atoms is thus modifying the low-energy region of the dynamics associated to motions of the neodymium and apical oxygen atoms in the (ab) plane. Figure 6 shows the histogram of displacements of the apical-plus-interstitial oxygen, the neodymium and the nickel atoms, computed from the AIMD trajectories of $\text{Nd}_2\text{NiO}_{4.0}$ and $\text{Nd}_2\text{NiO}_{4.25}$ using the PRM method [19]. There is an evident modification of the atomic displacements of the interstitial-and-apical oxygen atoms, from the $[100]$ direction in $\text{Nd}_2\text{NiO}_{4.0}$ toward the $[110]$ direction in $\text{Nd}_2\text{NiO}_{4.25}$. A similar trend, though less pronounced, is observed for the Nd atoms, which also show a higher displacement amplitudes in the (ab) plane in $\text{Nd}_2\text{NiO}_{4.25}$ than in $\text{Nd}_2\text{NiO}_{4.0}$. In comparison, the displacements of Ni atoms, while also showing higher displacement amplitudes in the overstoichiometric phase, remain isotropic in the (ab) plane. This shift in the direction of the atomic displacement of the apical, interstitial and neodymium atoms reflects an underlying modification of the shape of the potential energy surface in which these atoms sit. It is also consistent with the anisotropic stiffening of the lattice (cf. Fig. 2) that is more pronounced in the Γ – X than in the Γ – M direction.

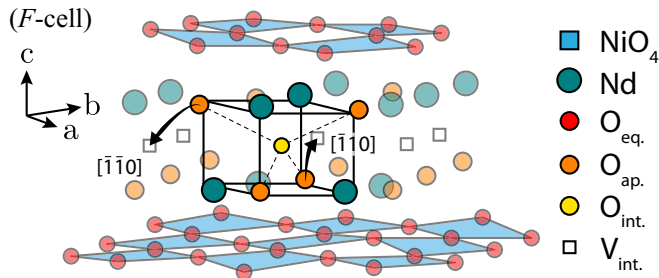


FIG. 7. Scheme of the $\text{Nd}_2\text{NiO}_{4+\delta}$ structure emphasizing the rock-salt layer. Equatorial O_{eq} , apical O_{ap} , and interstitial O_{int} oxygen atoms are marked by red, orange, and yellow circles, respectively; empty interstitial sites V_{int} are marked by white rectangles; neodymium atoms are marked by green circles; square-planar NiO_4 are colored in blue.

The change of direction of the oxygen motions toward $[110]$ upon incorporation of excess oxygen atoms, which then coincide with the direction of the diffusion pathway, is at the basis of the concept of phonon-assisted diffusion. By contrast to Fig. 1, which emphasizes a static description of the structure, we show in Fig. 7 an updated scheme of the structure accounting for the system dynamics. As it is clear that the apical oxygen atoms have their dynamics within the rock-salt layer, rather than being part of a rigid octahedra, a better description would be to consider the $\text{Nd}_2\text{NiO}_{4+\delta}$ structure as an intergrowth of rock-salt and square-planar NiO_4 layers. This description makes evident the static displacements and switch of the dynamics from the $[100]$ to the $[110]$ direction due to the presence of excess oxygen in interstitial site, and how the $[110]$ static and dynamic atomic displacements of the apical oxygen would favor diffusion events (marked as arrows in Fig. 7) toward empty neighboring interstitial sites.

D. Quasielastic scattering

The impact that the oxygen mobility may have on the lattice dynamics and its signature in the inelastic spectra are yet to be elucidated.

At ambient temperature, the activation of oxygen diffusion in $\text{Nd}_2\text{NiO}_{4+\delta}$ seems to be highly correlated with the amount of extra oxygen in interstitial sites and with the large displacements of the apical oxygen atoms toward interstitial sites themselves [18]. These two findings are not incompatible as the influence of the interstitial oxygen on the atomic motion anharmonicity and anisotropy were found to be subsided with increasing temperature by a more conventional thermal motion anharmonicity.

While a few diffusion events can be observed in the AIMD simulations at room temperature, the time spent by the apical and interstitial oxygen atoms diffusing is negligible compared to the time spent on the lattice sites. Moreover, such interstitial-apical diffusion is localized at room temperature (apical move to interstitial and then back to apical).

As a consequence, at room temperature and below, neither local nor long-range oxygen diffusion are expected to contribute in a significant manner to the dynamic response

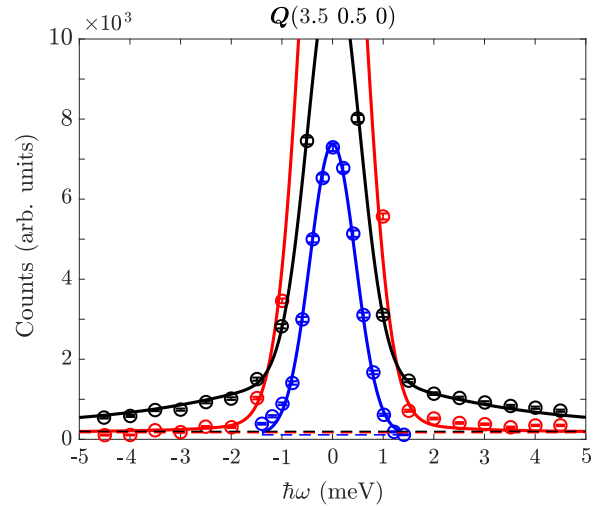


FIG. 8. Quasielastic scattering emerging from the tails of the elastic line at the generic Q point $(3.5\ 0.5\ 0)$. $\text{Nd}_2\text{NiO}_{4.25}$ at $T = 50$ K (red), $\text{Nd}_2\text{NiO}_{4.25}$ at 300 K (black), measured instrument resolution with a vanadium sample (blue).

of the sample in the inelastic channel. However, there were many attempts of diffusion events before one oxygen succeed in reaching the saddle point and had a chance to complete. All these attempts have associated simultaneous rearrangement of the structures. This means that even without effective long-range or localized diffusion, there are still structural immediate rearrangements in the timescale of the diffusion attempt. At room temperature, the diffusion attempt frequency must be on the same frequency range of the underlying lattice dynamics, which cooperatively works in periodically lowering the barrier for the diffusion, and so lies in the range of THz (i.e., time window of ps). Such dynamic rearrangement might enter the time window of IN8.

We checked for the occurrence of quasielastic scattering through a supplementary energy scan around the elastic line on IN8. At a generic hkl point $(3.5\ 0.5\ 0)$, which does not correspond to any structural or superstructure peak, we found that upon increasing the temperature from $T = 50$ K to 300 K, a quasielastic signal appears in the form of inelastic tails to the elastic line (Fig. 8). The fitting model consists of a delta function and a Lorentzian function, representing the elastic intensity and the quasielastic signal, respectively, convoluted to the Gaussian-shaped experimental resolution (blue line in Fig. 8). The fitted quasielastic signal has a half width at half maximum of 2.9 meV, which corresponds to dynamics on the timescale of a few picoseconds (1.4 ps). The quasielastic signal in the picosecond timescale is rationalized as fast local rearrangements in the $\text{Nd}_2\text{O}_{2+\delta}$ rock-salt layer, enabled by the shallowness of the apical oxygen and neodymium potentials and driven by the presence of excess oxygen in interstitial sites and their inherent dynamics. In comparison, the timescale of long-range oxygen diffusion at room temperature should be in the nanosecond range, which corresponds to a QENS broadening in the μeV -to-meV range that cannot be seen on IN8.

IV. CONCLUSIONS

We performed a detailed spectroscopic analysis of the dynamics of the overstoichiometric oxide $\text{Nd}_2\text{NiO}_{4.25}$, a complex system which combines well-defined incommensurate long-range ordering and a degree of dynamical local disorder from the distortions caused by the presence of excess oxygen in interstitial sites. Combining single-crystal neutron spectroscopy measurements of $\text{Nd}_2\text{NiO}_{4.25}$, harmonic phonon calculations, and AIMD simulations, we could explain the origin of several modification of the lattice and single-particle dynamics we pointed out upon incorporation of excess oxygen.

These modifications pertain mainly to the dynamics in the (ab) plane, while the coherent dynamics along the c direction (stacking direction) is marginally affected by the presence of interstitials. First, the acoustic branches measured experimentally at low q match those calculated for the parent stoichiometric compound, yet showing a stiffening of the longitudinal branch along the $[100]$ direction. At higher q values, toward the Brillouin zone boundary, the experimental observation deviates from the simulations and acoustic phonons sharply flattens and all phonons line shapes significantly broaden. This behavior is rationalized as a reduction of the correlation length of modes in space and time due to the disorder induced by excess oxygen atoms in interstitial sites. Despite the lack of evidence of phason modes developing from incommensurate satellites, the flattening and broadening of phonon modes toward the Brillouin zone boundaries is similar to that generally observed for other incommensurate phases.

Beyond phonon dispersions, the experimental spectra contained additional intensities that could not be explained when accounting only for one-phonon coherent scattering processes. This additional intensity, appearing as a broad nondispersive signal in the 5–15 meV region observed on all scans in the (ab) plane, was identified as single scattering incoherent inelastic scattering. This contribution was successfully reproduced in AIMD simulations of the $\text{Nd}_2\text{NiO}_{4.25}$ phase, and then attributed to the self-dynamics of Nd atoms.

Comparison with calculations of the stoichiometric parent compound evidenced a partial shift of the incoherent spectral weight from 5–10 meV toward 10–15 meV. This modification can only originate from the effect of the overstoichiometry and is rationalized as a modification of the distribution of

vibrational modes. Indeed, the Nd atoms close to interstitials see their movements along $[100]$ impeded due to the stiffening discussed above, while displacements along $[110]$ at higher energies are favored. Such findings parallel the results of our previous investigation where we assessed the same modification in dynamics for the apical oxygen from $[100]$ to $[110]$ displacements [18].

These results together evidence that the modification of the dynamics due to oxygen overstoichiometry is highly anisotropic along the layer planes and impacts to a great extent the rock-salt layer. The analysis of coherent and incoherent scattering highlights a marked anharmonicity of vibrational modes in the rock-salt layer. This is then the substructure involved in the dynamics disorder that sets on with temperature in the moderate temperature region, and likely to be the driving force for the push-pull diffusion mechanism in the (ab) plane.

This would be also in agreement with the high anisotropy found for diffusion measurements using the $^{18}\text{O}/^{16}\text{O}$ tracer method, where the diffusion in the (ab) plane has been determined to be at least three orders of magnitude higher compared to the c direction [70].

Finally, the timescale of the localized rearrangement motion of Nd, as a consequence of rearrangement of the whole structure upon oxygen insertion, becomes accessible in the quasielastic range with increasing temperature. Indeed, a quasielastic response is observed already at room temperature, when localized anaharmonic displacement of apical oxygen sets on, and is rationalized as the rearrangements in a timescale of few picoseconds of the rock-salt units close to the interstitials.

The combination of AIMD with single-crystal neutron spectroscopy turned out to be a powerful tool to explore disordered systems. Indeed, the AIMD allowed us here to extract both coherent and incoherent parts of the scattering function at specific Q points as a function of energy, and we were able to reproduce experimental data and relate them to the effect of overstoichiometry.

ACKNOWLEDGMENTS

MENESR financing the Ph.D. of A.P. is gratefully acknowledged. We also thank ILL for the beamtime on IN8 [71] and D19 [72] and the time on the computational cluster.

-
- [1] R. K. Lenka, P. K. Patro, V. Patel, L. Muhmood, and T. Mahata, *J. Alloys Compd.* **860**, 158490 (2021).
 - [2] D. Kim and K. T. Lee, *Ceram. Int.* **47**, 2493 (2021).
 - [3] A. Montenegro-Hernandez, J. Eduardo Vega-Castillo, A. Caneiro, and L. Moggi, *Solid State Ionics* **347**, 115093 (2020).
 - [4] E. Pikalova, A. Kolchugin, N. Bogdanovich, D. Medvedev, J. Lyagaeva, L. Vedmid, M. Ananyev, S. Plaksin, and A. Farlenkov, *Int. J. Hydrogen Energy* **45**, 13612 (2020).
 - [5] R. Dutta, A. Maity, A. Marsicano, M. Ceretti, D. Chernyshov, A. Bosak, A. Villesuzanne, G. Roth, G. Perversi, and W. Paulus, *J. Mater. Chem. A* **8**, 13987 (2020).
 - [6] S. Z. Xu, R. Jacobs, and D. Morgan, *Chem. Mater.* **30**, 7166 (2018).
 - [7] S. Saher, J. Song, V. Vibhu, C. Nicolle, A. Flura, J. M. Bassat, and H. J. M. Bouwmeester, *J. Mater. Chem. A* **6**, 8331 (2018).
 - [8] R. K. Sharma and E. Djurado, *J. Mater. Chem. A* **5**, 22277 (2017).
 - [9] R. K. Sharma, S. K. Cheah, M. Burriel, L. Dessemond, J. M. Bassat, and E. Djurado, *J. Mater. Chem. A* **5**, 1120 (2017).
 - [10] R. K. Sharma, M. Burriel, L. Dessemond, V. Martin, J. M. Bassat, and E. Djurado, *J. Power Sources* **316**, 17 (2016).

- [11] A. Egger, N. Schrodler, C. Gspan, and W. Sitte, *Solid State Ionics* **299**, 18 (2017).
- [12] D. M. Halat, R. Dervisoglu, G. Kim, M. T. Dunstan, F. Blanc, D. S. Middlemiss, and C. P. Grey, *J. Am. Chem. Soc.* **138**, 11958 (2016).
- [13] M. A. Laguna-Bercero, A. R. Hanifi, H. Monzon, J. Cunningham, T. H. Etsell, and P. Sarkar, *J. Mater. Chem. A* **2**, 9764 (2014).
- [14] V. Vibhu, A. Rougier, C. Nicollet, A. Flura, J. C. Grenier, and J. M. Bassat, *Solid State Ionics* **278**, 32 (2015).
- [15] T. Ogier, F. Mauvy, J. M. Bassat, J. Laurencin, J. Mougou, and J. C. Grenier, *Int. J. Hydrogen Energy* **40**, 15885 (2015).
- [16] C. Ferchaud, J. C. Grenier, Y. Zhang-Steenwinkel, M. M. A. van Tuel, F. P. F. van Berkel, and J. M. Bassat, *J. Power Sources* **196**, 1872 (2011).
- [17] F. Chauveau, J. Mougou, J. M. Bassat, F. Mauvy, and J. C. Grenier, *J. Power Sources* **195**, 744 (2010).
- [18] A. Perrichon, A. Piovano, M. Boehm, M. Zbiri, M. Johnson, H. Schober, M. Ceretti, and W. Paulus, *J. Phys. Chem. C* **119**, 1557 (2015).
- [19] A. Piovano, A. Perrichon, M. Boehm, M. R. Johnson, and W. Paulus, *Phys. Chem. Chem. Phys.* **18**, 17398 (2016).
- [20] S. R. Maity, M. Ceretti, L. Keller, J. Schefer, M. Meven, E. Pomjakushina, and W. Paulus, *Phys. Rev. Mater.* **5**, 014401 (2021).
- [21] A. Maity, R. Dutta, A. Marsicano, A. Piovano, J. R. Stewart, and W. Paulus, *Phys. Rev. B* **103**, L100401 (2021).
- [22] S. R. Maity, M. Ceretti, L. Keller, J. Schefer, T. Shang, E. Pomjakushina, M. Meven, D. Sheptyakov, A. Cervellino, and W. Paulus, *Phys. Rev. Mater.* **3**, 083604 (2019).
- [23] P. G. Freeman, M. Enderle, S. M. Hayden, C. D. Frost, D. X. Yao, E. W. Carlson, D. Prabhakaran, and A. T. Boothroyd, *Phys. Rev. B* **80**, 144523 (2009).
- [24] P. G. Freeman, R. A. Mole, N. B. Christensen, A. Stunault, and D. Prabhakaran, *Phys. B: Condens. Matter* **536**, 720 (2018).
- [25] J. M. Tranquada, D. J. Buttrey, V. Sachan, and J. E. Lorenzo, *Phys. Rev. Lett.* **73**, 1003 (1994).
- [26] A. Maity, R. Dutta, O. Sendtskiy, M. Ceretti, A. Lebranchu, D. Chernyshov, A. Bosak, and W. Paulus, *Chem. Mater.* **34**, 414 (2021).
- [27] T. Jarlborg and A. Bianconi, *J. Supercond. Novel Magn.* **29**, 615 (2016).
- [28] P. Odier, N. Poirot, P. Simon, and D. D. Meneses, *Eur. Phys. J.: Appl. Phys.* **5**, 123 (1999).
- [29] J. M. Tranquada, D. J. Buttrey, and D. E. Rice, *Phys. Rev. Lett.* **70**, 445 (1993).
- [30] D. J. Buttrey, J. D. Sullivan, G. Shirane, and K. Yamada, *Phys. Rev. B* **42**, 3944 (1990).
- [31] M. Ceretti, O. Wahyudi, A. Cousson, A. Villesuzanne, M. Meven, B. Pedersen, J. M. Bassat, and W. Paulus, *J. Mater. Chem. A* **3**, 21140 (2015).
- [32] M. Yashima, M. Enoki, T. Wakita, R. Ali, Y. Matsushita, F. Izumi, and T. Ishihara, *J. Am. Chem. Soc.* **130**, 2762 (2008).
- [33] M. Ceretti, O. Wahyudi, G. Andre, M. Meven, A. Villesuzanne, and W. Paulus, *Inorg. Chem.* **57**, 4657 (2018).
- [34] A. Chroneos, D. Parfitt, J. A. Kilner, and R. W. Grimes, *J. Mater. Chem.* **20**, 266 (2010).
- [35] D. Parfitt, A. Chroneos, J. A. Kilner, and R. W. Grimes, *Phys. Chem. Chem. Phys.* **12**, 6834 (2010).
- [36] D. Price, M. Saboungi, and F. Bermejo, *Rep. Prog. Phys.* **66**, 407 (2003).
- [37] P.-F. Lory, V. M. Giordano, P. Gille, H. Euchner, M. Mihalkovic, E. Pellegrini, M. Gonzalez, L.-P. Regnault, P. Bastie, H. Schober, S. Pailhes, M. R. Johnson, Y. Grin, and M. de Boissieu, *Phys. Rev. B* **102**, 024303 (2020).
- [38] P.-F. Lory, S. Pailhes, V. M. Giordano, H. Euchner, H. D. Nguyen, R. Ramlau, H. Borrmann, M. Schmidt, M. Baitinger, M. Ikeda, P. Tomes, M. Mihalkovic, C. Allio, M. R. Johnson, H. Schober, Y. Sidis, F. Bourdarot, L. P. Regnault, J. Ollivier, S. Paschen, Y. Grin, and M. de Boissieu, *Nat. Commun.* **8**, 491 (2017).
- [39] Y. Bouyrie, C. Candolfi, S. Pailhes, M. M. Koza, B. Malaman, A. Dauscher, J. Tobola, O. Boisson, L. Saviot, and B. Lenoir, *Phys. Chem. Chem. Phys.* **17**, 19751 (2015).
- [40] C. Stock, P. M. Gehring, G. Xu, D. Lamago, D. Reznik, M. Russina, J. Wen, and L. A. Boatner, *Phys. Rev. B* **90**, 224302 (2014).
- [41] M. M. Koza, M. R. Johnson, R. Viennois, H. Mutka, L. Girard, and D. Ravot, *Nat. Mater.* **7**, 805 (2008).
- [42] M. M. Koza, L. Capogna, A. Leithe-Jasper, H. Rosner, W. Schnelle, H. Mutka, M. R. Johnson, C. Ritter, and Y. Grin, *Phys. Rev. B* **81**, 174302 (2010).
- [43] P. M. Gehring, H. Hiraka, C. Stock, S. H. Lee, W. Chen, Z. G. Ye, S. B. Vakhrushev, and Z. Chowdhuri, *Phys. Rev. B* **79**, 224109 (2009).
- [44] V. Keppens, D. Mandrus, B. Sales, B. Chakoumakos, P. Dai, R. Coldea, M. Maple, D. Gajewski, E. Freeman, and S. Bennington, *Nature (London)* **395**, 876 (1998).
- [45] D. J. Voneshen, K. Refson, E. Borissenko, M. Krisch, A. Bosak, A. Piovano, E. Cemal, M. Enderle, M. J. Gutmann, M. Hoesch, M. Roger, L. Gannon, A. T. Boothroyd, S. Uthayakumar, D. G. Porter, and J. P. Goff, *Nat. Mater.* **12**, 1028 (2013).
- [46] H. Liu, X. Shi, F. Xu, L. Zhang, W. Zhang, L. Chen, Q. Li, C. Uher, T. Day, and G. J. Snyder, *Nat. Mater.* **11**, 422 (2012).
- [47] D. J. Voneshen, H. C. Walker, K. Refson, and J. P. Goff, *Phys. Rev. Lett.* **118**, 145901 (2017).
- [48] S. Danilkin, A. Skomorokhov, A. Hoser, H. Fuess, V. Rajevac, and N. Bickulova, *J. Alloys Compd.* **361**, 57 (2003).
- [49] M. K. Gupta, J. Ding, D. Bansal, D. L. Abernathy, G. Ehlers, N. C. Osti, W. G. Zeier, and O. Delaire, *Adv. Energy Mater.* **12**, 2200596 (2022).
- [50] G. L. Squires, *Introduction to the Theory of Thermal Neutron Scattering* (Cambridge University Press, Cambridge, 1978).
- [51] O. Wahyudi, M. Ceretti, I. Weill, A. Cousson, F. Weill, M. Meven, M. Guerre, A. Villesuzanne, J. M. Bassat, and W. Paulus, *CryStengcomm* **17**, 6278 (2015).
- [52] See Supplemental Material at <http://link.aps.org/supplemental/10.1103/PhysRevB.107.144303> for Fig.S1 picture of the grown single-crystal; Fig. S2 diffraction maps on $(hk0)$ plane; Fig. S3 inelastic neutron spectra though satellite peaks; Fig. S4 calculated phonon dispersion from DFT; Fig. S5 analysis of the effect of twinning on inelastic neutron scattering; Table S1 fitted parameter of Fig. S5; Table S2 low energy phonon modes and polarizations from DFT; Fig. S6 correspondence of reciprocal points between F -cell and supercell; Table S3 list of selected correspondence points in Fig. S6; design of non-stoichiometric model.
- [53] G. M. Sheldrick, *Acta Crystallogr. Sec. C* **71**, 3 (2015).

- [54] M. Kempa, B. Janousova, J. Saroun, P. Flores, M. Boehm, F. Demmel, and J. Kulda, *Phys. B: Condens. Matter* **385**, 1080 (2006).
- [55] G. Kresse and J. Hafner, *Phys. Rev. B* **48**, 13115 (1993).
- [56] G. Kresse and J. Hafner, *Phys. Rev. B* **49**, 14251 (1994).
- [57] G. Kresse and J. Furthmüller, *Comput. Mater. Sci.* **6**, 15 (1996).
- [58] G. Kresse and J. Furthmüller, *Phys. Rev. B* **54**, 11169 (1996).
- [59] P. E. Blöchl, *Phys. Rev. B* **50**, 17953 (1994).
- [60] G. Kresse and D. Joubert, *Phys. Rev. B* **59**, 1758 (1999).
- [61] J. P. Perdew, K. Burke, and M. Ernzerhof, *Phys. Rev. Lett.* **77**, 3865 (1996).
- [62] S. Nosé, *J. Chem. Phys.* **81**, 511 (1984).
- [63] S. Nosé, *Prog. Theor. Phys. Suppl.* **103**, 1 (1991).
- [64] D. M. Bylander and L. Kleinman, *Phys. Rev. B* **46**, 13756 (1992).
- [65] G. Goret, B. Aoun, and E. Pellegrini, *J. Chem. Inf. Model.* **57**, 1 (2017).
- [66] K. Parlinski, Z. Q. Li, and Y. Kawazoe, *Phys. Rev. Lett.* **78**, 4063 (1997).
- [67] J. D. Axe, M. Iizumi, and G. Shirane, *Phys. Rev. B* **22**, 3408 (1980).
- [68] M. Iizumi, J. D. Axe, G. Shirane, and K. Shimaoka, *Phys. Rev. B* **15**, 4392 (1977).
- [69] M. de Boissieu, *Chem. Soc. Rev.* **41**, 6778 (2012).
- [70] J. M. Bassat, P. Odier, A. Villesuzanne, C. Marin, and M. Pouchard, *Solid State Ionics* **167**, 341 (2004).
- [71] doi:10.5291/ILL-DATA.7-01-345.
- [72] doi:10.5291/ILL-DATA.5-11-400.